arXiv:2205.07423v1 [astro-ph.SR] 16 May 2022

# Quasi-periodic Accelerations of Energetic Particles during a Solar Flare

Dong Li, and Wei Chen

*Key Laboratory of Dark Matter and Space Astronomy, Purple Mountain Observatory, CAS, Nanjing 210023, PR China*

## ABSTRACT

We report the observation of non-stationary Quasi-Periodic Pulsations (QPPs) in high-energy particles during the impulsive phase of an X4.8 flare on 2002 July 23 (SOL2002-07-23T00:35). The X4.8 flare was simultaneously measured by the Reuven Ramaty High Energy Solar Spectroscopic Imager, Nobeyama Radio Polarimeters, and Nobeyama Radioheliograph. The quasi-period of $\sim$50$\pm$15 s, determined by the wavelet transform, is detected in the $\gamma$-ray line emission. Using the same method, a quasi-period of $\sim$90$\pm$20 s is found in $\gamma$-ray continuum, hard X-ray (HXR) and radio emissions during almost the same time. Our observations suggest that the flare QPPs should be associated with energetic ions and nonthermal electrons that quasi-periodically accelerated by the repetitive magnetic reconnection. The different quasi-periods between $\gamma$-ray line and continuum/HXR/radio emissions indicate an apparent difference in acceleration or propagation between energetic ions and nonthermal electrons of this solar flare.

*Subject headings:* Solar flares — Solar oscillations — Solar gamma-ray emission — Solar X-ray emission — Solar radio emission

## 1. Introduction

Solar observations in $\gamma$-ray, hard X-ray (HXR), and radio emissions have provided useful diagnostics for particle accelerations of energetic ions and electrons on the solar system (Aschwanden 2002; Vilmer et al. 2011). Solar energetic particles, such as nonthermal electrons and energetic ions, can interact with the solar atmosphere and then produce radio (i.e. microwave), HXR, $\gamma$-ray line and continuum emissions. Some energetic particles may escape into the interplanetary space, generating the low-frequency radio emission. The acceleration of electron beams in solar flares has been established by detecting the radio, HXR, and $\gamma$-ray continuum radiation, while the corresponding acceleration of high-energy ions during large flares was prompted by measuring the nuclear $\gamma$-ray line emission (e.g. Vilmer 2012). Spectroscopic observations in high-energy channels have probed the behavior of sub-relativistic and relativistic charged particles (i.e. ions and electrons)

Correspondence should be sent to: lidong@pmo.ac.cn

during solar flares, such as the neutron-capture line at 2223 keV, the positron-electron annihilation line at 511 keV, and the prompt de-excitation $\gamma$-ray lines of heavy particles (Chupp 1983; Lin et al. 2003; Share et al. 2003; Smith et al. 2003; Gan 2005; Murphy et al. 2007; Chen & Gan 2020). The $\gamma$-ray line centered at 2223 keV is quite strong and extremely narrow, it is generated when the thermalized neutron captured by the ambient proton, regarded as the deuterium formation line. This strong $\gamma$-ray line can be used as an indicator of $\gamma$-ray flares, reflecting the radiation of nuclear reactions involving flare-accelerated ions, and it has been well studied using the imaging and spectroscopy observations, especially at the Reuven Ramaty High Energy Solar Spectroscopic Imager (RHESSI; Lin et al. 2002) era, i.e., line shapes, line fluences, time histories and spatially-resolved locations (e.g. Holman et al. 2003; Hurford et al. 2003; Krucker et al. 2003; Lin et al. 2003; White et al. 2003; Emslie et al. 2004; Dauphin & Vilmer 2007; Chen & Gan 2012). While the quasi-periodic pulsations (QPPs) of this strong $\gamma$-ray line during solar flares have been rarely reported.

QPPs are frequently observed as temporal intensity fluctuations during solar/stellar flares (see Van Doorsselaere et al. 2016; Zimovets et al. 2021a, for reviews). They are often characterized by a series of irregular but repetitive pulsations, termed as 'non-stationary QPPs' (e.g. Nakariakov et al. 2019). Generally, a typical QPP event should have at least three successive peaks. Because it is unnecessary to discuss the periodic behavior if there are only one or two peaks, which might be just a coincidence, for instance, the similar time interval between successive peaks occurred by chance (Nakariakov et al. 2019; Li 2022a). The flare-related QPPs have been detected almost in the whole solar spectrum, i.e., radio/micowaves, white lights, H$\alpha$, ultraviolet/extreme ultraviolet (UV/EUV), Ly$\alpha$, soft/hard X-rays (SXR/HXR) and $\gamma$-rays (e.g. Nakariakov et al. 2010; Li et al. 2020a,b; Clarke et al. 2021; Hong et al. 2021; Kashapova et al. 2021; Zhao et al. 2021; Karlický et al. 2022; Li 2022b; Shi et al. 2022). The observed quasi-periods are varied from sub-seconds to several tens of minutes (Melnikov et al. 2005; Ning 2017; Hayes et al. 2020; Karlický & Yasnov 2021; Zimovets et al. 2021b; Howard & MacGregor 2022; Ning et al. 2022; Shen et al. 2022; Zhou et al. 2022). Here, the quasi-period refers to a slight variation of the dominant period. The characteristic duration of all peaks in one QPP, regarded as the period, is expected to be equal. However, the durations in observations are mostly varied and irregular, and thus regarded as 'quasi-period' (cf. Nakariakov et al. 2018). The quasi-period of a flare QPP is often associated with its generation mechanism. Usually, the short-period QPP, such as $<1$ s, could be related to the dynamic interaction of plasma waves with ambient energetic particles in the complex magnetic structure (Tan et al. 2010; Karlický et al. 2022), and the long-period QPPs, i.e., $>1$ s, are frequently explained as magnetohydrodynamic (MHD) waves (Nakariakov & Kolotkov 2020). The flare QPP can also be driven by the repetitive magnetic reconnection that can periodically accelerate electrons and ions, and the quasi-period of reconnection process may be either spontaneous or triggered (Nakariakov et al. 2018; Yuan et al. 2019; Clarke et al. 2021; Li et al. 2021; Karampelas et al. 2022). In a recent review article (e.g. Zimovets et al. 2021a), a total of about fifteen mechanisms/models were proposed to interpret flare QPPs. However, it is still an open issue for the generation mechanism of flare QPPs, mainly because that our observations cannot satisfy

all the necessary requirements to determine one mechanism that should be responsible for a specific QPP event.

Thanks to the RHESSI HXR and $\gamma$-ray imaging and spectroscopy observations, the X4.8 flare on 2002 July 23 had been analyzed in many papers. For example, Lin et al. (2003) presented an overview of this flare observations, Hurford et al. (2003) constructed the first $\gamma$-ray maps, Krucker et al. (2003) investigated the movement of HXR sources, White et al. (2003) compared the images between radio and HXR emissions produced by high-energy electrons, Holman et al. (2003) analyzed the high-resolution HXR spectra, Smith et al. (2003) measured line profiles of de-excitation lines generated by energetic ions, Murphy et al. (2003) and Share et al. (2003) reported spectral observations of the neutron-capture line at 2223 keV and the positron-electron annihilation line at 511 keV, respectively. However, the quasi-periodicity, especially the $\gamma$-ray QPP, has not been reported during the X4.8 flare. In this letter, we investigated non-stationary QPPs in $\gamma$-ray line and continuum, HXR, and radio emissions during the flare impulsive phase. Our observations revealed that the quasi-period detected in $\gamma$-ray line emission was deviated from that observed in $\gamma$-ray continuum, HXR, and radio emissions, suggesting that the accelerated or propagated processes of energetic ions and nonthermal electrons should be a bit different.

## 2. Observations

On 2002 July 23, an intense flare occurred in the active region of NOAA 10039 near the solar east limb, i.e., S13E72. It was simultaneously measured by the Geostationary Operational Environmental Satellite (GOES), RHESSI (Lin et al. 2002), Nobeyama Radio Polarimeters (NoRP) and Nobeyama Radioheliograph (NoRH; Nakajima et al. 1994), as shown in Figure 1. Panel (a) plots the GOES SXR flux at 1−8 Å from 00:10 UT to 01:40 UT, which indicates an X4.8-class flare. The X4.8 flare began at ∼00:18 UT and peaked at about 00:35 UT in the GOES flux, as marked by the vertical orange lines. The GOES flare was accompanied by a group of type III radio bursts, as shown by the context image measured by Wind/Waves at the low-frequency range of 0.02−13.825 MHz.

RHESSI can provide SXR, HXR and $\gamma$-ray imaging spectroscopy of solar flares from 3 keV to 17 MeV (Lin et al. 2002). Figure 1 (b) presents the full-disk light curves in HXR emissions at 50−100 keV (black) and 100−300 keV (red), as well as in $\gamma$-ray emissions at 300−500 keV (magenta), 700−1400 keV (green), and 2200−2300 keV (blue), respectively. They have been normalized by their maximum values, and some light curves have been shifted in height to display clearly in a same window. Their time cadence is 4 s. To improve the signal-to-noise (SN) ratio, the $\gamma$-ray line flux where the 2223 keV line completely dominated, was integrated over a wide energy range of 100 keV, and thus we can obtain sufficient photon counts for QPP test. The HXR maps were reconstructed by the RHESSI team and can be directly downloaded from the RHESSI Image

Archive[1]. Here, we used HXR maps with the CLEAN algorithm. On the other hand, it is impossible to reconstruct the $\gamma$-ray map without the help of RHESSI team. Herein, we used the centroid locations of $\gamma$-ray line and continuum emissions obtained by Hurford et al. (2003). We wanted to state that the RHESSI light curves during about 00:26−00:35 UT were in a same attenuator[2]. So, the HXR and $\gamma$-ray fluxes during our observations were not affected by the RHESSI attenuator changes.

NoRH was designed to measure solar radio maps with a time cadence of 1 s at frequencies of 17 GHz and 34 GHz. However, there were some data gap during our observations, resulting into some discontinuities when integrated over light curves. Thus, the NoRH light curve was unable to be used for QPP test. On the other hand, NoRP could provide solar radio fluxes with an uniform resolution of 0.1 s at seven frequencies, such as 1 GHz, 2 GHz, 3.75 GHz, 9.4 GHz, 17 GHz, 35 GHz, and 80 GHz. Figure 1 (c) shows solar radio fluxes normalized to their maximum values at three higher frequencies recorded by NoRP during 00:25−00:33 UT. The X4.8 flare was also observed by the Michelson Doppler Imager (MDI) on board the Solar and Heliospheric Observatory (SOHO) and the Transiton Region and Coronal Explorer (TRACE) at 195 Å, which provided the full-disk magnetograms and EUV maps, respectively.

## 3. Methods and Results

In Figure 1, the flare light curves in $\gamma$-rays, HXR, and radio emissions are dominated by several successive peaks, which appear to be irregular but repetitive. Thus, they could be considered as a good candidate for non-stationary QPPs. It can be seen that a sharp dip appears at roughly 00:30:20 UT, as indicated by the red arrow. The sharp dip can be observed in $\gamma$-rays, HXR, and radio fluxes, implying that some flare-accelerated electrons/ions escaped from the Sun and propagate into the interplanetary space. The synchronous low-frequency type III radio burst observed by Wind/Waves in Figure 1 (a) confirmed the presence of escaping electrons. We also note that the sharp dip of $\gamma$-ray line flux is later than that of HXR and radio fluxes, which is consistent with previous findings by comparing their temporal profiles or the times of peak flux (e.g. Lin et al. 2003; Share et al. 2003; Dauphin & Vilmer 2007; Vilmer et al. 2011), for instance, a time delay of about 12 s was found between the $\gamma$-ray line flux and the HXR flux at 150 keV (cf. Share et al. 2003; Vilmer et al. 2011).

In order to take a closer look at the flare QPP in $\gamma$-ray emissions, we performed a wavelet transform technique with the mother function of 'Morlet' (Torrence & Compo 1998). Figure 2 presents the Morlet wavelet analysis results in $\gamma$-ray emissions during the impulsive phase of the X4.8 flare. The upper panels show flare light curves during ∼00:25−00:33 UT in $\gamma$-ray line (a1) and continuum

[1]https://hesperia.gsfc.nasa.gov/rhessi_extras/flare_images/2002/07/23/20020723_0018_0116/hsi_20020723_0018_0116.html

[2]http://hessi.ssl.berkeley.edu/hessidata/metadata/2002/07/22/hsi_20020722_235720_rate.png

(a2 and a3) emissions, respectively. Similar to previous studies (e.g. Nakariakov et al. 2010; Li et al. 2020a), the raw light curves (black) were firstly running average by smoothing 25 points (100-s window). Thus, we obtained the slow-varying trends, as indicated by the overplotted cyan lines. Next, the detrended fluxes in panels (b1)−(b3) were derived from the raw light curves after subtracting their slow-varying trends. Both the raw and detrended light curves in $\gamma$-ray continuum emissions at 700−1400 keV and 300−500 keV appear at least three successive peaks from roughly 00:27 UT to 00:31 UT, while the successive peaks in the $\gamma$-ray line emission seem to be more than three during the same time interval, suggesting a short quasi-period. Moreover, the modulation depths of these peaks, regarded as the ratio of the oscillatory amplitude to their maximum slow-varying trend, are roughly 20%−25%, which is consistent with what was found by Nakariakov et al. (2010). Finally, the Morlet wavelet transform technique was applied to those detrended light curves, as shown in panels (c1)−(c3). These Morlet wavelet power spectra reveal an enhanced power over a broad range of periods, indicating the presence of QPPs at $\gamma$-ray levels. The bulk of power spectra suggests that the flare QPP is characterized by a dominant period within a large error. The dominant period is determined from the center of enhanced power, while the error is simply identified from the boundary of a 99.9% significance level. The quasi-period in $\gamma$-ray line emission is estimated to about 50±15 s, while that in $\gamma$-ray continuum emissions is around 90±20 s. Obviously, the quasi-periods in $\gamma$-ray line and continuum emissions are different.

Figure 3 presents Morlet wavelet analysis results in HXR and radio emissions observed by RHESSI and NoRP, respectively. Panels (a1)−(a3) draw the raw light curves (black) and their slow-varying trends (cyan). Here, the HXR light curve was smoothed by 25 points, while the radio fluxes were smoothed by 1000 points, and thus their smoothing window has a same temporal scale of 100 s, same to that in $\gamma$-ray fluxes. Panels (b1)−(b3) plot the detrended light curves after removing the slow-varying trends from their raw light curves. Similar to the $\gamma$-ray continuum emission, both HXR and radio fluxes exhibit about three large-scale peaks from roughly 00:27 UT to 00:31 UT. The modulation depths of those peaks in HXR 50−100 keV and radio 17 GHz are estimated to be 20%−30%, roughly in agreement with those found in $\gamma$-ray light curves. While the modulation depth in radio 80 GHz is much smaller, i.e., only 1%−2%. On the other hand, the HXR and radio fluxes appear a number of sub-peaks with very small amplitudes during our observations, which is different from that in $\gamma$-ray emissions, and thus it is beyond the scope of this study. Panels (c1)−(c3) show the Morlet wavelet power spectra, revealing an enhanced power over a broad range of periods, which is estimated to about 90±20 s. This quasi-period matches well with that seen in $\gamma$-ray continuum emissions, but it is larger than that found in the $\gamma$-ray line emission.

To look closely the spectral structure of the flare QPPs, we constructed wavelet amplitude spectra (Torrence & Compo 1998; Torrence & Webster 1999; Karlický et al. 2020). Figure 4 shows the amplitude wavelet spectra constructed from the detrended time profiles in $\gamma$-ray line and continuum emissions, as well as the HXR and radio emissions, the superimposed magenta contour in each panel represents a significance level of 99.9%. In panel (a), there is a periodicity with an av-

erage period of about 50 s inside the 99.9% significance level, confirming the presence of 50-s QPP in the $\gamma$-ray line emission. In panels (b)−(f), a periodicity with an average period near 90 s is seen inside the 99.9% significance level, suggesting the synchronous presence of a dominant period at $\sim$90 s in $\gamma$-ray continuum, HXR and radio emissions. The quasi-periods of those oscillations are all manifested as bright and dark patches in the amplitude wavelet spectra, similarly to what observed with the flare QPPs in radio, EUV and X-ray emissions (cf. Karlický et al. 2020). On the other hand, the average period in the $\gamma$-ray line is obvious smaller than that seen in $\gamma$-ray continuum, HXR and radio emissions, in agreement with the quasi-period seen in the wavelet power spectra.

The difference in QPP periods between $\gamma$-ray line and HXR/radio emissions might be related to their source locations in the solar surface, as shown in Figure 5. Panels (a) and (b) present HXR and radio maps with a field-view-of (FOV) of $\sim 100'' \times 100''$ during the X4.8 flare, which is also in the QPP duration. Here, the HXR maps were reconstructed by the RHESSI team using the CLEAN algorithm, and we downloaded them from the RHESSI Image Archive. The overlaid contours were obtained from the RHESSI data in the energy range of 50−100 keV (yellow) and 100−300 keV (red), the NoRP data at frequencies of 17 GHz (orange) and 34 GHz (cyan). The contour levels are set at 30%, 60% and 90%, respectively. It can be seen that the two HXR source locations match well with each other, and their locations are roughly consistent with the radio source region, which is similar to previous observations (White et al. 2003). The slight divergence could because that the HXR emission above 50 keV tends to appear in the double footpoint locations, while the radio emission in 17 GHz is dominated by the loop-top source, and the radio emission in 34 GHz moves closely to the footpoint locations.

Figure 5 (c) shows the line-of-sight (LOS) magnetogram with a same FOV observed by SOHO/MDI during the X4.8 flare. Panel (d) draws the EUV 195 Å map captured by TRACE after the X1.4 flare, since the TRACE maps were severe saturated during the intense flare. The overlaid contours are made from the HXR 50−100 keV (yellow) and radio 17 GHz (orange) or 34 GHz (cyan) emissions at the level of 30%, similarly to what have been shown in Figure 5 (a) and (b). The overplotted circles represent the source sites of flare $\gamma$-ray emissions at 2218−2228 keV (gold), 700−1400 keV (green), and 300−500 keV (magenta), respectively. It should be pointed out that the $\gamma$-ray source locations are referenced from Hurford et al. (2003) and Lin et al. (2003), because we cannot restructure the $\gamma$-ray maps of a solar flare. As reported by Hurford et al. (2003), the centroid locations of $\gamma$-ray continuum emissions at 700−1400 keV and 300−500 keV were coincident with that of the HXR emission at 50−100 keV. Moreover, they were both overlaid on the radio sources at 17 GHz and 34 GHz. On the other hand, the $\gamma$-ray line centroid position was located away from the HXR and radio sites, implying that the acceleration region of energetic ions was displaced from the corresponding site of nonthermal electrons, i.e., a departure of $\sim 20 \pm 6''$ (cf. Hurford et al. 2003; Lin et al. 2003). The EUV map after the X4.8 flare exhibits a series of postflare loops, as shown in Figure 5 (d). Although the $\gamma$-ray line centroid position was not located near any clear EUV or H$\alpha$ brightening (cf. Lin et al. 2003; Vilmer et al. 2011), it was actually sited at the footpoint of a outer and larger postflare loop, while the $\gamma$-ray continuum centroid locations

matched with inner and smaller loops. All those observations suggest that the propagation process or acceleration sites of energetic ions and electron beams might be significantly displaced in the solar flare. The location differences between $\gamma$-ray line and continuum as well as HXR/radio emissions are consistent with their variations in quasi-periods.

## 4. Summary and Discussion

We reported the observation of non-stationary QPPs in the $\gamma$-ray line emission during the impulsive phase of an X4.8 flare on 2002 July 23. The intense flare was well studied in the early era of RHESSI, such as: reconstructed maps in $\gamma$-ray and HXR emissions (Hurford et al. 2003; Krucker et al. 2003; Lin et al. 2003; White et al. 2003), Doppler redshifts and line broadening of heavy particles (Smith et al. 2003), spectral measurements in HXR, $\gamma$-ray line and continuum emissions (Holman et al. 2003; Murphy et al. 2003; Share et al. 2003). On the other hand, the quasi-periodicity of this flare was not yet investigated in detail. In order to simultaneously obtain the high temporal cadence and SN ratio, we used a broad energy range (i.e., 100 keV) to integrate the $\gamma$-ray line flux with a time bin of 4 s. In the previous study (e.g. Hurford et al. 2003), a narrow energy range (i.e., 10 keV) but a low time cadence such as 40 s was applied to improve the SN ratio. Herein, we could detect the quasi-period of 50$\pm$15 s in the $\gamma$-ray line emission. Previous observations (e.g. Chupp 1983; Nakariakov et al. 2010; Li et al. 2020a) have showed the presence of QPP features in $\gamma$-ray light curves during solar flares. However, these studies covered much broader energy ranges, such as 4100$-$6400 keV (Chupp 1983) and 2000$-$6000 keV (Nakariakov et al. 2010), or they just based on the $\gamma$-ray continuum emission at a lower energy range, i.e., 331$-$1253 keV (e.g. Li et al. 2020a). To the best of our knowledge, this is the first detailed study of flare QPPs in $\gamma$-ray line emission at around 2223 keV.

The flare QPP with a quasi-period of 90$\pm$20 s was observed in $\gamma$-ray continuum emissions at 300$-$500 keV and 700$-$1400 keV during the same impulsive phase. The same 90-s QPP was also seen in the HXR emission at 50$-$100 keV, and radio emissions at frequencies of 17 GHz and 80 GHz. In fact, the HXR emission at 100$-$300 keV and radio emission at 35 GHz also showed the similar 90-s QPP, as shown in Figure 1 (b) and (c). Our observation was consistent with the observational result from the $\gamma$-ray and HXR maps, for instance, the centroid locations of $\gamma$-ray continuum emissions roughly coincided with the source regions of HXR and radio emissions (cf. Hurford et al. 2003; White et al. 2003). All those observational facts suggested that the $\gamma$-ray continuum emission at lower energy was dominated by the electron bremsstrahlung radiation, similar to the HXR emission (Vilmer et al. 2011; Vilmer 2012). The modulation depth of the flare QPP was estimated to 20%$-$30% in $\gamma$-ray and HXR emissions, in agreement with what was found by Nakariakov et al. (2010) in microwave, HXR and $\gamma$-ray time series. The similar modulation depth was also detected in radio emissions at frequencies of 17 GHz and 35 GHz. However, the modulation depth in radio 80 GHz was much smaller, i.e., only 1%$-$2%, which could be attributed to the strong background emission and low SN ratio.

The flare QPPs were simultaneously observed in $\gamma$-ray line and continuum, HXR and radio emissions, implying a common origin of the flare-accelerated ions and electrons, for instance, they were both likely accelerated by the repetitive magnetic reconnection during the flare impulsive phase. Our observations support the idea that the acceleration process of energetic ions and nonthermal electrons were linked to each other in the solar flare. On the other hand, the quasi-period seen in the $\gamma$-ray line emission was visual shorter than that found in $\gamma$-ray continuum, HXR and radio emissions, suggesting that there were some variations in acceleration or propagation process between energetic ions and electron beams, which had been confirmed by the spatial-resolved imaging observation, for instance, the neutron-capture line location was displaced by $\sim 20 \pm 6''$ from the source region of electron beams (e.g. Hurford et al. 2003; Lin et al. 2003; Vilmer et al. 2011).

The flare QPPs can be modulated by several mechanisms, i.e., the global kink-mode or sausage-mode waves (Nakariakov & Kolotkov 2020). They both could cause changes of the magnetic-mirror ratio, and then drive quasi-periodic precipitations of energetic ions and nonthermal electrons in flare/coronal loops (e.g. Foullon et al. 2005; Nakariakov et al. 2010). Hence, their quasi-periods ($P$) are usually associated with loop lengths ($L$) and the Alfvén speed ($V_A$) outside the loop, such as $P \approx 2L/V_A$. If we assumed a semi-circular shape for the flare loop (Tian et al. 2016), the short-loop length was estimated to 31 Mm, and the long-loop length was roughly equal to 53 Mm. Thus, the 90-s QPP observed in HXR and radio emissions in the short flare loop requires a Alfvén speed of $\sim$700 km s$^{-1}$, while the 50-s QPP seen in the $\gamma$-ray line emission in the long flare loop needs a Alfvén speed of $\sim$2100 km s$^{-1}$. These speeds are slower than the typical speed estimated in the global sausage oscillation, such as 3000$-$5000 km s$^{-1}$ (Nakariakov et al. 2003; Melnikov et al. 2005), but they are roughly close to the phase speed of global kink oscillations in flare loops (Foullon et al. 2005). On the other hand, the quasi-period of 50 s seen in the $\gamma$-ray line emission was associated with a large postflare loop (e.g. Lin et al. 2003), similarly to what was found by Dauphin & Vilmer (2007) that energetic ions were injected in larger loops than nonthermal electrons. However, our observation contradicted the previous finding that the quasi-period of kink oscillations was proportional to the major length of coronal loops (e.g. Anfinogentov et al. 2015). Therefore, there must be effective mechanisms/models whereby energetic ions were preferentially accelerated in larger flare loops, such as: the stochastic acceleration mechanism (e.g. Emslie et al. 2004), or the trap-plus-precipitation model (e.g. Dauphin & Vilmer 2007). All those considerations therefore support a probable interpretation of flare QPPs: they can be driven by the repetitive magnetic reconnection that are likely to be triggered by global kink-mode oscillations, and then produce quasi-periodic particle accelerations, for instance, periodically accelerated energetic ions and nonthermal electrons (Foullon et al. 2005; Nakariakov et al. 2010). Of course, the flare QPPs could be caused by the other repetitive magnetic reconnection, i.e., modulated by a self-induced oscillation (Zimovets et al. 2021a). So far, we cannot exclude or demonstrate this possibility, largely due to the absence of quantitative theories and high-resolution observations.

The authors thank the anonymous referee for his/her valuable comments and suggestions. We thank the teams of RHESSI, NoRP, NoRH, WIND, TRACE, and SOHO/MDI for their open data

use policy. This work is funded by the National Key R&D Program of China 2021YFA1600502 (2021YFA1600500), NSFC under grants 11973092, U1931138, 12073081, 11820101002, as well as CAS Strategic Pioneer Program on Space Science, Grant No. XDA15052200, XDA15320300, and XDA15320301. D. Li is also supported by the Surface Project of Jiangsu Province (BK20211402).

## REFERENCES

Anfinogentov, S. A., Nakariakov, V. M., & Nisticò, G. 2015, A&A, 583, A136. doi:10.1051/0004-6361/201526195

Aschwanden, M. J. 2002, Space Sci. Rev., 101, 1. doi:10.1023/A:1019712124366

Chupp, E. L. 1983, Sol. Phys., 86, 383. doi:10.1007/BF00157212

Chen, W. & Gan, W.-Q. 2012, Research in Astronomy and Astrophysics, 12, 1439. doi:10.1088/1674-4527/12/10/006

Chen, W. & Gan, W. Q. 2020, ApJ, 895, 8. doi:10.3847/1538-4357/ab886c

Clarke, B. P., Hayes, L. A., Gallagher, P. T., et al. 2021, ApJ, 910, 123. doi:10.3847/1538-4357/abe463

Dauphin, C. & Vilmer, N. 2007, A&A, 468, 289. doi:10.1051/0004-6361:20066247

Emslie, A. G., Miller, J. A., & Brown, J. C. 2004, ApJ, 602, L69. doi:10.1086/382350

Foullon, C., Verwichte, E., Nakariakov, V. M., et al. 2005, A&A, 440, L59. doi:10.1051/0004-6361:200500169

Gan, W. Q. 2005, Advances in Space Research, 35, 1833. doi:10.1016/j.asr.2004.11.025

Hayes, L. A., Inglis, A. R., Christe, S., et al. 2020, ApJ, 895, 50. doi:10.3847/1538-4357/ab8d40

Holman, G. D., Sui, L., Schwartz, R. A., et al. 2003, ApJ, 595, L97. doi:10.1086/378488

Hong, Z., Li, D., Zhang, M., et al. 2021, Sol. Phys., 296, 171. doi:10.1007/s11207-021-01922-1

Howard, W. S. & MacGregor, M. A. 2022, ApJ, 926, 204. doi:10.3847/1538-4357/ac426e

Hurford, G. J., Schwartz, R. A., Krucker, S., et al. 2003, ApJ, 595, L77. doi:10.1086/378179

Kashapova, L. K., Kolotkov, D. Y., Kupriyanova, E. G., et al. 2021, Sol. Phys., 296, 185. doi:10.1007/s11207-021-01934-x

Karampelas, K., McLaughlin, J. A., Botha, G. J. J., et al. 2022, ApJ, 925, 195. doi:10.3847/1538-4357/ac3b53

Karlický, M., Kašparová, J., & Sych, R. 2020, ApJ, 888, 18. doi:10.3847/1538-4357/ab5801

Karlický, M. & Yasnov, L. V. 2021, A&A, 646, A179. doi:10.1051/0004-6361/202039850

Karlický, M., Rybak, J., Benacek, J., et al. 2022, arXiv:2204.09327

Krucker, S., Hurford, G. J., & Lin, R. P. 2003, ApJ, 595, L103. doi:10.1086/378840

Li, D., Kolotkov, D. Y., Nakariakov, V. M., et al. 2020a, ApJ, 888, 53. doi:10.3847/1538-4357/ab5e86

Li, D., Feng, S., Su, W., et al. 2020b, A&A, 639, L5. doi:10.1051/0004-6361/202038398

Li, D., Ge, M., Dominique, M., et al. 2021, ApJ, 921, 179. doi:10.3847/1538-4357/ac1c05

Li, D. 2022a, arXiv:2204.02047

Li, D. 2022b, Sci. China Tech. Sci., 65, 139. doi:10.1007/s11431-020-1771-7

Lin, R. P., Dennis, B. R., Hurford, G. J., et al. 2002, Sol. Phys., 210, 3. doi:10.1023/A:1022428818870

Lin, R. P., Krucker, S., Hurford, G. J., et al. 2003, ApJ, 595, L69. doi:10.1086/378932

Melnikov, V. F., Reznikova, V. E., Shibasaki, K., et al. 2005, A&A, 439, 727. doi:10.1051/0004-6361:20052774

Murphy, R. J., Share, G. H., Hua, X.-M., et al. 2003, ApJ, 595, L93. doi:10.1086/378175

Murphy, R. J., Kozlovsky, B., Share, G. H., et al. 2007, ApJS, 168, 167. doi:10.1086/509637

Nakajima, H., Nishio, M., Enome, S., et al. 1994, IEEE Proceedings, 82, 705

Nakariakov, V. M., Melnikov, V. F., & Reznikova, V. E. 2003, A&A, 412, L7. doi:10.1051/0004-6361:20031660

Nakariakov, V. M., Foullon, C., Myagkova, I. N., et al. 2010, ApJ, 708, L47. doi:10.1088/2041-8205/708/1/L47

Nakariakov, V. M., Kolotkov, D. Y., Kupriyanova, E. G., et al. 2019, Plasma Physics and Controlled Fusion, 61, 014024. doi:10.1088/1361-6587/aad97c

Nakariakov, V. M., Anfinogentov, S., Storozhenko, A. A., et al. 2018, ApJ, 859, 154. doi:10.3847/1538-4357/aabfb9

Nakariakov, V. M. & Kolotkov, D. Y. 2020, ARA&A, 58, 441. doi:10.1146/annurev-astro-032320-042940

Ning, Z. 2017, Sol. Phys., 292, 11. doi:10.1007/s11207-016-1037-4

Ning, Z., Wang, Y., Hong, Z., et al. 2022, Sol. Phys., 297, 2. doi:10.1007/s11207-021-01935-w

Share, G. H., Murphy, R. J., Skibo, J. G., et al. 2003, ApJ, 595, L85. doi:10.1086/378174

Shen, Y., Zhou, X., Duan, Y., et al. 2022, Sol. Phys., 297, 20. doi:10.1007/s11207-022-01953-2

Shi, F., Li, D., & Ning, Z. 2022, Universe, 8, 104. doi:10.3390/universe8020104

Smith, D. M., Share, G. H., Murphy, R. J., et al. 2003, ApJ, 595, L81. doi:10.1086/378173

Tan, B., Zhang, Y., Tan, C., et al. 2010, ApJ, 723, 25. doi:10.1088/0004-637X/723/1/25

Tian, H., Young, P. R., Reeves, K. K., et al. 2016, ApJ, 823, L16. doi:10.3847/2041-8205/823/1/L16

Torrence, C. & Compo, G. P. 1998, Bulletin of the American Meteorological Society, 79, 61. doi:10.1175/1520-0477(1998)079<0061:APGTWA>2.0.CO;2

Torrence, C. & Webster, P. J. 1999, Journal of Climate, 12, 2679. doi:10.1175/1520-0442(1999)012<2679:ICITEM>2.0.CO;2

Van Doorsselaere, T., Kupriyanova, E. G., & Yuan, D. 2016, Sol. Phys., 291, 3143. doi:10.1007/s11207-016-0977-z

Vilmer, N., MacKinnon, A. L., & Hurford, G. J. 2011, Space Sci. Rev., 159, 167. doi:10.1007/s11214-010-9728-x

Vilmer, N. 2012, Philosophical Transactions of the Royal Society of London Series A, 370, 3241. doi:10.1098/rsta.2012.0104

White, S. M., Krucker, S., Shibasaki, K., et al. 2003, ApJ, 595, L111. doi:10.1086/379274

Yuan, D., Feng, S., Li, D., et al. 2019, ApJ, 886, L25. doi:10.3847/2041-8213/ab5648

Zhao, J., Liu, W., & Vial, J.-C. 2021, ApJ, 921, L26. doi:10.3847/2041-8213/ac3339

Zhou, X., Shen, Y., Liu, Y. D., et al. 2022, arXiv:2204.05603

Zimovets, I. V., McLaughlin, J. A., Srivastava, A. K., et al. 2021a, Space Sci. Rev., 217, 66. doi:10.1007/s11214-021-00840-9

Zimovets, I., Sharykin, I., & Myshyakov, I. 2021b, Sol. Phys., 296, 188. doi:10.1007/s11207-021-01936-9

This preprint was prepared with the AAS LaTeX macros v5.2.

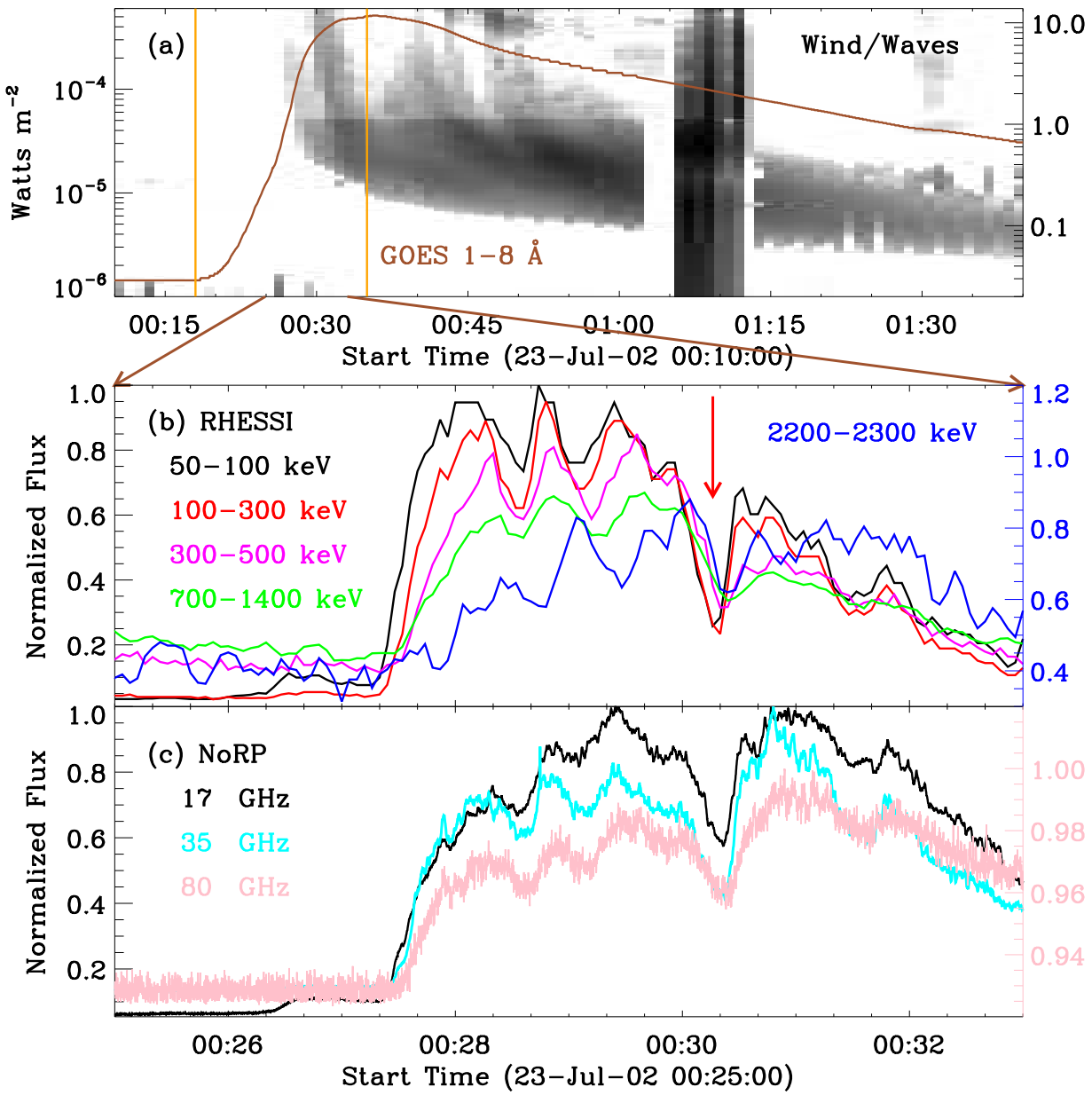


Fig. 1.— (a): Radio dynamic spectrum measured by Wind/Waves. The overplotted light curve is recorded by GOES 1−8 Å from 00:10 UT to 01:40 UT. The vertical orange lines mark the start and peak times of the X4.8 flare. (b): Normalized HXR and $\gamma$-ray fluxes between 00:25 UT and 00:33 UT observed by RHESSI in energy ranges of 50−100 keV (black), 100−300 keV (red), 300−500 keV (magenta), 700−1400 keV (green), and 2200−2300 keV (blue). (c): Normalized radio fluxes during 00:25−00:33 UT measured by NoRP at frequencies of 17 GHz (black), 35 GHz (cyan), 80 GHz (pink).

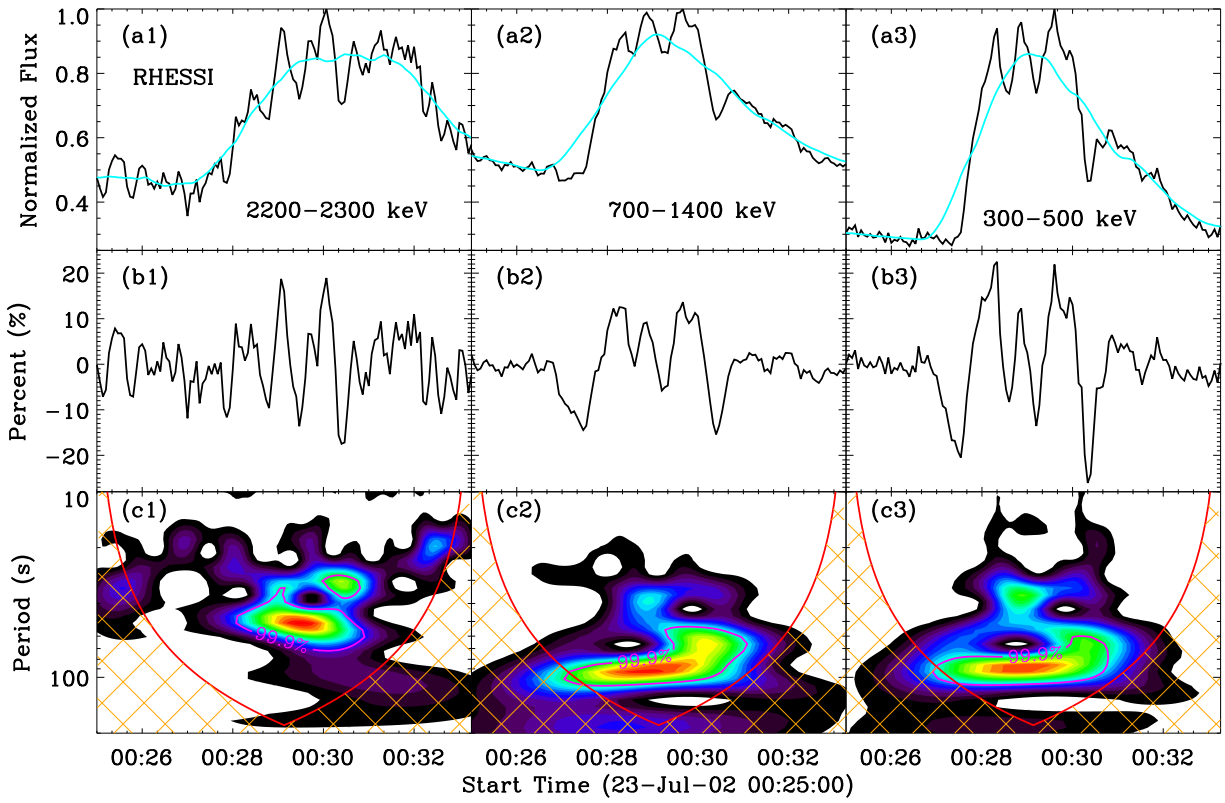


Fig. 2.— (a1−a3) Flare fluxes normalized to their maximum values in $\gamma$-ray line and continuum emissions observed by RHESSI (black), the overlaid cyan lines are their slow-varying trends. (b1−b3) Detrended light curves normalized to their maximum slow-varying trends. (c1−c3) Morlet wavelet power spectra. The magenta contours indicate a significance level of 99.9%.

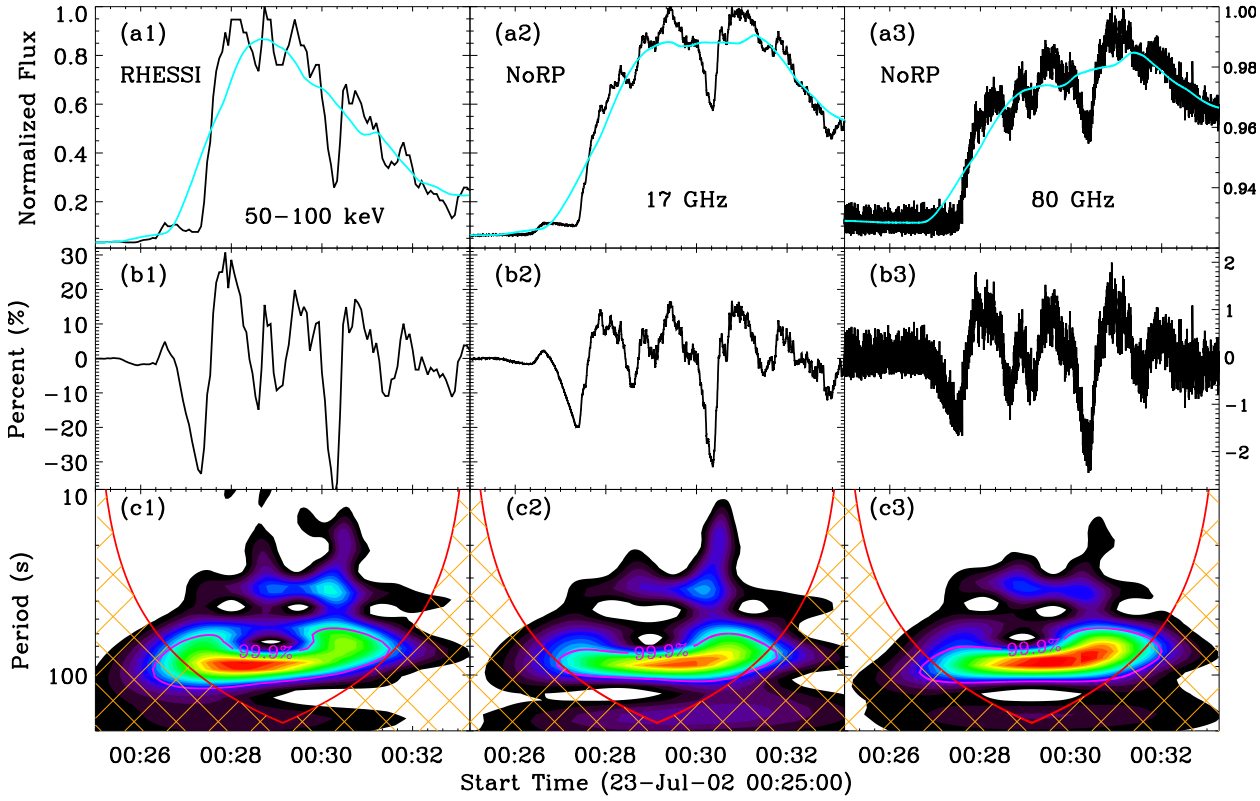


Fig. 3.— Similar to Figure 2, but for HXR and radio light curves in the energy range of RHESSI 50−100 keV, and at frequencies of NoRP 17 GHz and 80 GHz.

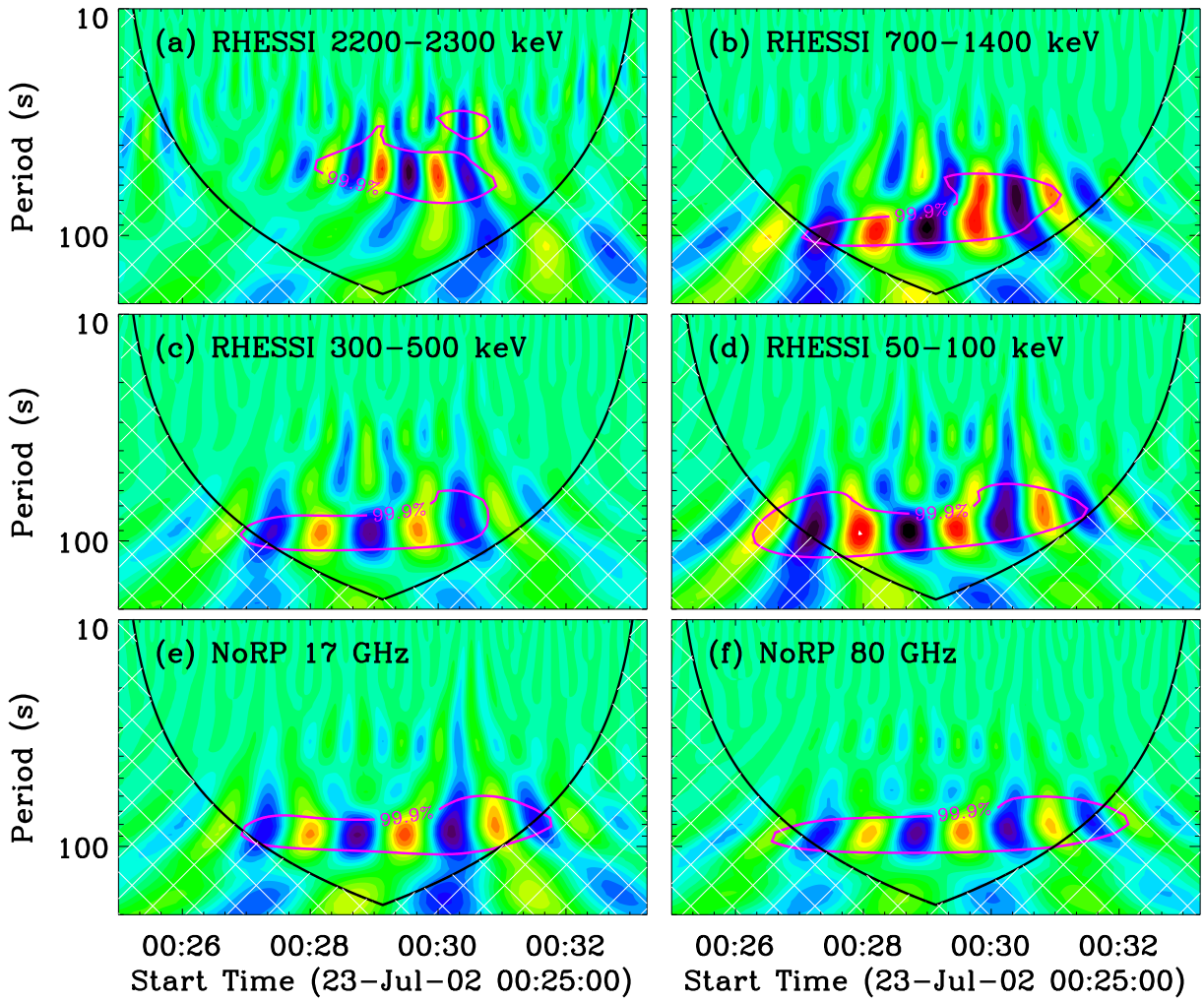


Fig. 4.— Wavelet amplitude spectra corresponding to the detrended time profiles seen in multiple wavelengths. The magenta contours represent the 99.9% significance level, and the color background indicates the signal variations in time and periods.

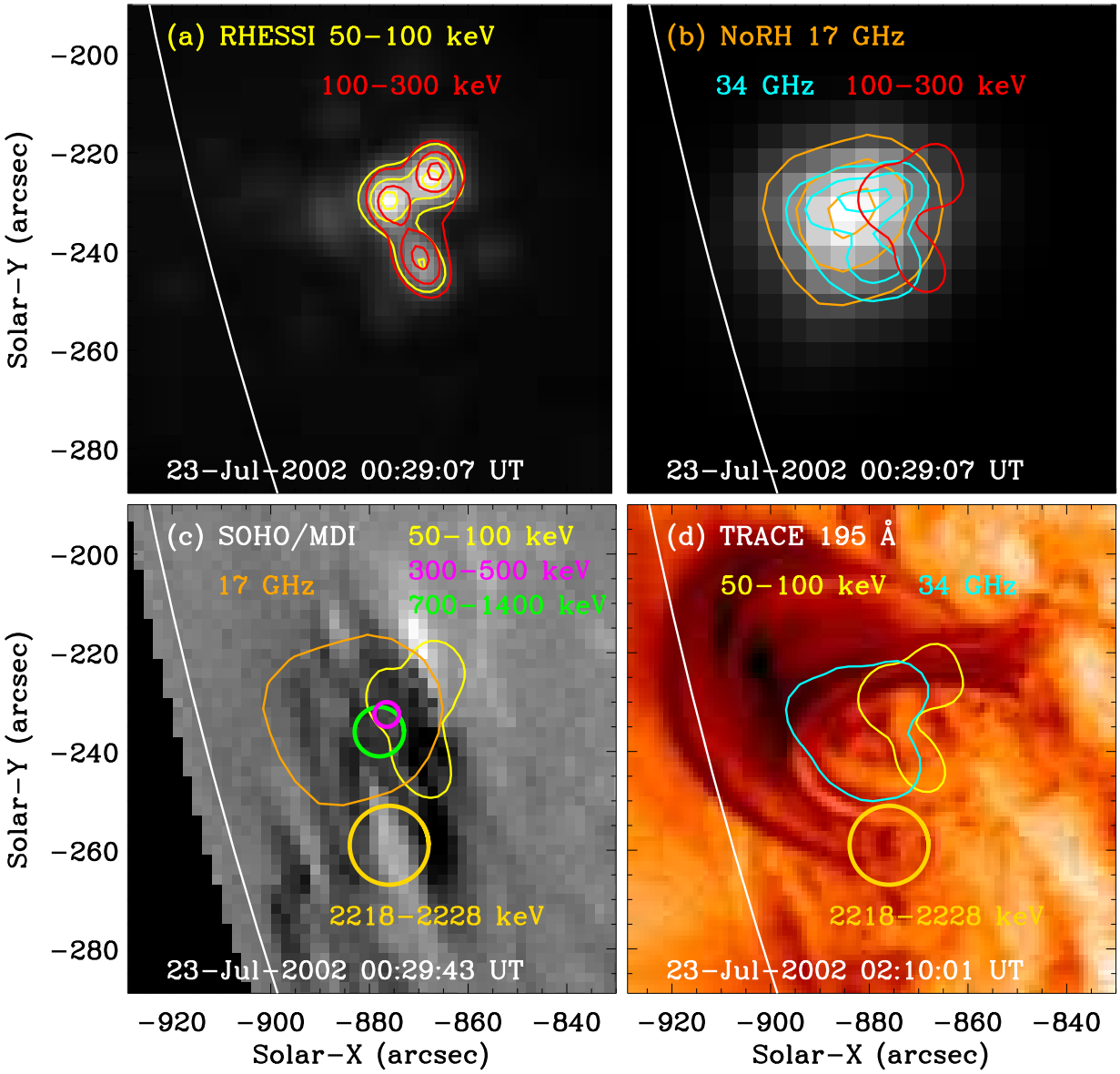


Fig. 5.— Imaging observations of the X4.8 flare with a FOV of $\sim 100'' \times 100''$. The background images are measured by RHESSI 50−100 keV (a), NoRH 17 GHz (b), SOHO/MDI (c), and TRACE 195 Å (d), respectively. The overlaid contours represents HXR and radio emissions derived from RHESSI 50−100 keV (yellow) and 100−300 keV (red), as well as NoRP 17 GHz (orange) and 34 GHz (cyan). Their levels are set at 30%, 60% and 90%. The circles represent the source locations (cf. Hurford et al. 2003; Lin et al. 2003) of RHESSI 300−500 keV (magenta), 700−1400 keV (green), and 2218−2228 keV (gold).